NUCET NUCLEAR ENERGY AND TECHNOLOGY

Nuclear Energy and Technology 10(3): 189–198
DOI 10.3897/nucet.10.129596

Research Article

Interaction of iron melt with tungsten and WFe composite structure evolution

Nikita Popov[1], Alexey Suchkov[1], Mikhail Zharkov[1,2], Veronika Kirillova[1], Alexander Bazhenov[1], Ivan Fedotov[1], Irina Bajenova[3], Alexandra Khvan[3], Ilya Kozlov[1,4], Alexey Vertkov[2], Oleg Sevryukov[1]

1 *National Research Nuclear University MEPhI (Moscow Engineering Physics Institute), Kashirskoye Shosse, 31, 115409 Moscow, Russia*

2 *Joint-Stock Company "N.A. Dollezhall Research and Development Institute of Power Engineering", (JSC "NIKIET"), Malaya Krasnoselskaya 2/8, 107140, Moscow, Russia*

3 *Faculty of Chemistry, Lomonosov Moscow State University, 1-3 Leninskiye Gory, 119991, Moscow, Russia*

4 *National Research Center "Kurchatov Institute", Moscow 123182, Russia*

Corresponding author: Nikita Popov (NSPopov@mephi.ru)

Academic editor: Tan Xiaoyue ♦ **Received** 12 June 2024 ♦ **Accepted** 07 August 2024 ♦ **Published** 27 August 2024

Citation: Popov N, Suchkov A, Zharkov M, Kirillova V, Bazhenov A, Fedotov I, Bajenova I, Khvan A, Kozlov I, Vertkov A, Sevryukov O (2024) Interaction of iron melt with tungsten and WFe composite structure evolution. Nuclear Energy and Technology 10(3): 189–198. https://doi.org/10.3897/nucet.10.129596

Abstract

Development of new plasma facing components (PFC) draw attention of numerous scientific groups in fusion energy field. Tungsten as a main PFC material main have poor machinability, thus various designs were proposed to overcome this problem. However, such technologies as functional graded layers, sintering and additive technologies are limited in production size and have low cost-efficiency. This research considers the alternative approach of steel melt injection or melt infiltration of tungsten mesh. The results obtained establish the mechanism of phase evolution during interaction of solid W with liquid steel and iron. Energy dispersive spectroscopy, X-ray diffraction and Thermocalc calculations used to analyze the phase composition of tungsten wetted with various steels and pure iron. Results show that interaction rate significantly depends on melt temperature and overheating above its liquidus. Then the overheating exceeds 150 °C erosion of tungsten occur.

Keywords

iron, steel, tungsten, composite, melting, wetting angle, high temperature interaction, intermetallic compounds, armor block, heat transfer

Introduction

Modern fusion facilities face the problem of erosion and sputtering of plasma facing components (PFC) material under thermal loads, which cause plasma contamination. Tungsten is proposed as a divertor material for International Thermonuclear Reactor (ITER) due to its high melting temperature, which allows it to withstand thermal loads up to 20 MW/m^2 (Hirai et al. 2005; Schoofs and Gorley 2019; Gago et al. 2020). Moreover, beryllium as the ITER first wall material will be replaced by tungsten due to its high sputtering rate (Guseva et al. 1999). However, some problems with tungsten armored blocks need to be resolved before their industrial application in the next generation fusion reactors.

High thermal conductivity of tungsten (Tolias 2017) provides high efficiency of heat transfer from the plasma-facing surface to the coolant. However, poor machinability of tungsten increases production costs. Joining tungsten blocks to the basic structure of a fusion facility by

high-temperature brazing requires high precision during the joining process. Experience in brazing technology shows that the gaps between materials should be about few dozens of microns (Bachurina et al. 2021a, 2021b; Penyaz et al. 2021). These production difficulties lead to a more complex design of a fusion facility. Alternative way to join W is hot isostatic pressing also require precision to provide acceptable performance (Saito et al. 2002).

On the other hand, Reduced Activation Ferritic-Martensitic (RAFM) steel and austenitic steel 316LN are commonly used as a base structural material for the ITER-like facilities. Steel can be easily cut, welded, and brazed. A combination of high thermal conductivity and machinability could be achieved in a composite material. In terms of technological simplicity, the WFe composite should consist of tungsten fiber, which transfers the heat, and an iron-based matrix, which allows the underlying structure to be cut and welded.

Another important point is that capillary porous systems (CPS), commonly made from various tungsten or molybdenum meshes, require a base material (Lyublinski et al. 2016). The Fig. 1 shows a schematic representation of WFe composite in tokamak construction with CPS and without. The WFe composite design implies that the plasma-facing surface of PFC made of tungsten or CPS will absorb heat load and transfer it to underlying WFe composite, which in turn transfer it to coolant. The liquid lithium technique show high performance in numerous experiments (Zuo et al. 2011; Yang et al. 2017; Andruczyk et al. 2020). As CPS is based on tungsten mesh, the WFe composite is a suitable base structure for it.

The WFe composite is designed to provide better performance than conventional copper and bronze elements, which unable to withstand high heat loads and radiation damage (Fabritsiev et al. 1996). The composite structure is compatible with liquid metal coolants with high thermal conductivity such as Li (Meng et al. 2018). To sum up, WFe could provide the thermal conductivity at the level of bronze and higher strength, while compatibility with liquid metal coolants allow absorbing higher heat fluxes.

The combination of W and steel in one material is a poorly developed topic primarily due to great difference between their CTE (α (W) = 4.4 × 10^{-6} K^{-1} and α (RAFM) = 12.7 × 10^{-6} K^{-1} (Paúl et al. 2006) and brittle intermetallic compounds (IMC) formation. In order to overcome this problem, materials with functional graded layers produced by plasma or magnetron sputtering have been proposed in works (Weber et al. 2013; Tan et al. 2019; Ganesh et al. 2023). This technique provides high adhesion between layers, yet low tolerance to cyclic loads cause failure after just a few cycles (Qu et al. 2019). In addition sintered layers of different materials are prone to interact due to diffusion with intermetallic Fe_7W_6 formation (Heuer et al. 2020).

Tungsten and steel powders joined by spark plasma sintering into a bulk material promise high thermal properties with minimal interaction between materials. Some positive results have been obtained in this field (Chen et al. 2018; Koller et al. 2018). However, Fe_2W type IMCs have been detected in the interaction layer between powder particles, which reduces thermal conductivity and mechanical properties. In general, sintering and functional graded layer approaches have low cost-efficiency and are limited in product size.

Additive technologies have a low production speed, but the current technology level allows us to control the structure of the material with high precision. Laser metal deposition of Fe and W powders was used to fabricate a WFe composite in the work (Chen et al. 2021). Microstructure investigation shows that numerous tungsten particles surrounded by an Fe_7W_6 layer are embedded in an iron matrix enriched with tungsten. Fe_2W intermetallic compounds nucleate in the steel matrix only upon multiple heating. Hence, it can be concluded that a short-term manufacturing process allows us to avoid the formation of an intermetallic phase.

The tungsten fiber mesh forms a capillary structure that can be easily filled with liquid steel. Infiltration with a liquid phase leads to a high interaction rate between materials. Alloys with low melting point and high oxidation resistance can be cast via different methods. Recently, the

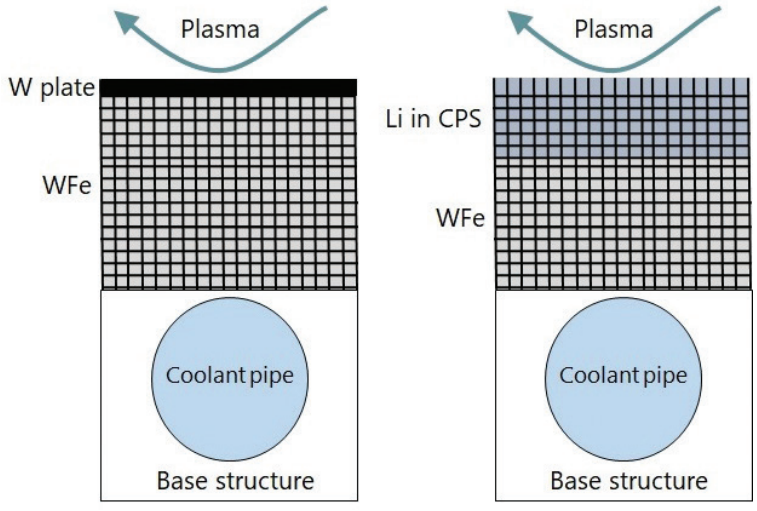

Figure 1. Schematic representation of WFe composite in PFC.

high-pressure die casting method has been significantly improved by the total vacuum process high-pressure die casting (EVP HPDC) (Gao et al. 2021). This technology makes it possible to obtain oxygen-sensitive amorphous Zr-based alloys with high glass-forming ability. The main difficulty for steel casting using EVP HPDC is the shot sleeve and die material, which will suffer from overheated steel melt. The main advantage of this technology is a high cooling rate almost high as in magnetic-pulse welding (Lazurenko et al. 2024).

The capillary forces could simplify the casting technique. Melt infiltration widely used to produce composites with ceramic or metal reinforcement (Toy and Scott 1990; Dandliker et al. 1998; De Jongh and Eggenhuisen 2013). When the melt interacts with the tungsten mesh, the liquid metal will be drawn in by capillary forces, forming a bulk solid structure reinforced with tungsten. The technology described above is similar to melt infiltration. Such technology have been already tested on W-Cu material for mock-ups of the limiter (De Luca et al. 2023).

The capillary force depends on the wetting characteristics of the liquid steel and the tungsten. The study of interaction between the liquid and solid materials and the following phase formation at high temperatures is important for the development of melt infiltration technology. The wetting behavior of steel melt on metal materials is poorly investigated. Few works consider the ceramic substrates wetted by steel and iron (Xuan et al. 2015; Yan et al. 2018; Long et al. 2024).

An attempt to manufacture the steel matrix strengthened with tungsten wire was made in (Kumar 2013). Casting at 1550 °C cause significant erosion and tungsten dissolution in steel melt. Due to the nature of casting various zones of composite have different structure with relatively thin and thick intermetallic layer. Thus, the critical temperature of melt when an interaction become intensive should be defined to achieve the desirable structure.

In this work, we made an attempt to investigate the features of the interaction at high temperatures of pure iron, several grades of steel, and a pure tungsten substrate. The data obtained is crucial for the melt infiltration technology, with regard to the WFe composite production.

Materials and methods

The investigation consists of two stages: wetting measurement and high-temperature interaction. The list of materials and their chemical composition according to manufacturer certificate given in Table 1. In all the experiments, pure ITER-grade tungsten was used as the base solid material. A simplified setup was used to represent the interaction between solid W and liquid steel during melt infiltration. The schematic experimental setups of stages 1 and 2 are shown in Fig. 2.

This study investigated the interaction of pure Fe, AISI 420, EK-181, and 316L steels with a pure tungsten substrate. The convenient sessile drop method was used in first stage of experiments. The steel and iron with a volume of approximately 64 mm^3 were placed on 20×20×2 mm tungsten plates. The tungsten substrates were ground with sandpaper (120–2500) and polished with diamond paste (3 and 1 μm) prior to the experiments. Both steel and tungsten were cleaned in alcohol in an ultrasonic bath to remove surface pollution that could affect the liquid-solid interaction.

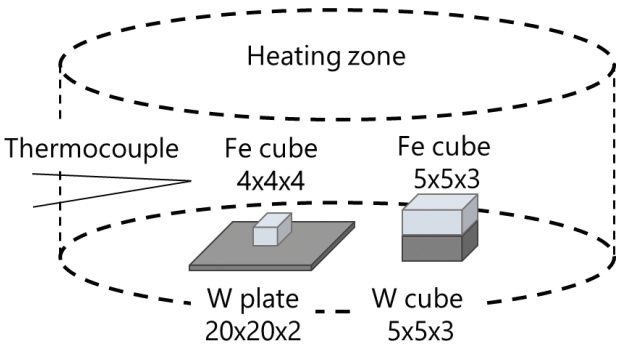

Figure 2. Schematic setup of wetting and interaction experiments.

The specimens were heated to the exposure temperature (T_{EX}) in a vacuum resistance furnace with a heating rate of about 18 °C/min. The heating modes and material properties are listed in Table 2. The exposure time was set at 1 and 10 minutes, and the vacuum level was maintained lower than 5×10^{-5} Torr. Cooling with a furnace follows after exposure. The cooling rate from T_{EX} to 1300 was approximately 100 °C/min, it decrease exponentially with a time. The wetting angle was studied after cooling to the room temperature in a furnace. The heating modes were designed to simulate the interaction of molten steel with tungsten fibers in the composite. As steel AISI 316L has the lowest melting point, it was also melted at 1500 °C. In this case exposure was excluded to simulate short-term interaction conditions. The temperature measurement error was about ±10 °C.

The second stage was dedicated to the study of microstructure and phase formation during high-temperature interaction. Steel, iron, and tungsten were cut into 5×5×3 mm pieces, and the heating conditions were the

Table 1. Materials chemical composition

Material	Content, wt.%							
	Fe	Cr	C	Ni	Ti	Mo	W	Other
Fe	>99.96	–	<0.035	–	–	–	–	–
AISI 420	Bal.	12–14	0.16–0.25	<0.6	–	–	–	<0.6Mn
EK-181	Bal.	10–12	0.12–0.18	–	0.05	0.01	2	0.006B; 0.2–0.4V; 0.05–0.2Ta
AISI 316L	Bal.	16–18	0.02	10–14	0.05	2–3	–	–
W	–	–	–	–	–	–	>99.99	0.01(Fe+P+O_2)

Table 2. Heating modes and material properties

Material	Solidus (T_S), °C	Liquidus (T_L), °C	Exposure temperature (T_{EX}), °C
Fe	1539		1550, 1600
AISI 420	1450	1510	1550, 1600
EK-181	1503	1513	1550, 1600
AISI316L	1375	1400	1500, 1550, 1600

same as in stage 1. Specimens of molten steel on tungsten were prepared according to the conventional method for studying microstructures. The specimens were named as follows: "WSteel/exposure temperature/exposure time", for example: W316/1500/1. The microstructure was examined via Scanning Electron Microscopy (SEM) using the JEOL JSM–6610LV. Qualitative elemental analysis was performed using Energy Dispersive Spectrometry (EDS) on the Oxford Instruments INCA x-act.

The phase composition was analyzed using X-ray diffraction (XRD) on a Brucker D8 Discover. Detecting small components of the structure was challenging due to technical limitations. To increase the accuracy of phase identification the local transient synchrotron XRD with a wavelength of 0.75 Å was used. Thermodynamic calculations were performed using Thermo-Calc software with the TCFE10 database. The phase composition at room temperature was calculated based on the local chemical analysis of specimens melted at 1550 °C.

Results and discussion

Wetting of tungsten substrate by steels and iron

To measure the wetting characteristics, the specimens were heated to the T_{EX} above their melting point. Exposure for 1 and 10 minutes ensured complete melting of the steel and iron. After cooling, each tungsten plate was completely wetted by the steel and iron, as the liquid metal wet the front and back sides of the tungsten plate. Consequently, there was no way to measure the contact angle, as it equaled zero. The results of the wetting experiments are illustrated in the photo in Fig. 3.

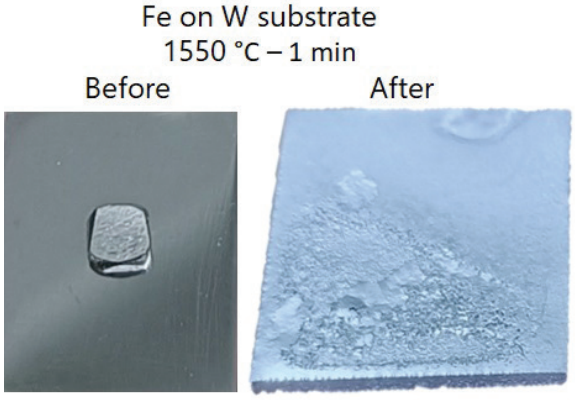

Figure 3. Tungsten plate before wetting and after wetting by iron at 1550 °C.

Long exposure times at T_{EX} significantly higher than T_L, followed by cooling and crystallization, may affect the results. At a temperature of 1500 °C, steel 316L was overheated by 100 °C above the liquidus temperature. The total time in liquid state is the sum of heating time (4 min for heating from T_L to 1500), exposure time (1 min) and cooling time (~1 min), which gives us 7 min.

The iron has a fixed melting point while steels melt in a certain temperature interval. The exposure temperature of 1550 °C is 11 °C higher than the melting point of pure iron. In this case, the total time in the liquid state was 2 minutes. The differences in chemical composition, melting points, and exposure times between the two considered cases do not affect the wetting process. It can be concluded that Fe-based materials wet tungsten well at a temperature range of steel and iron melting point. This characteristic is advantageous for utilizing capillary forces to form a composite structure.

Features of interaction between tungsten and steel melt

Interaction between W and Fe

The phase composition and structure of the joint significantly impact the final properties of the composite material. The formation of brittle phases during high-temperature interaction is critical for the mechanical properties of the composite. Iron forms two IMCs with tungsten: μ (Fe_7W_6) and Laves λ (Fe_2W). These phases are expected to form when liquid steel fills the capillaries in the tungsten mesh. A binary Fe-W phase diagram is presented in Fig. 4.

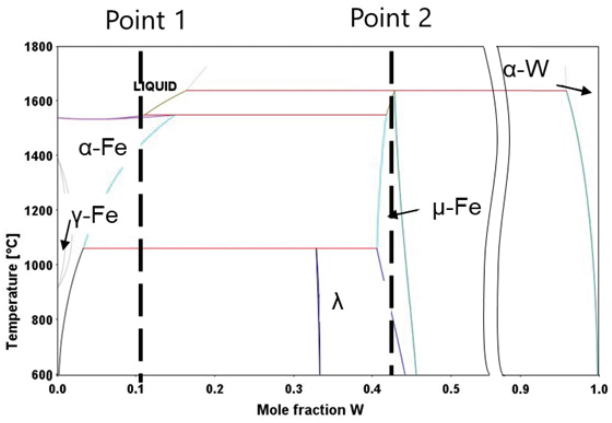

Figure 4. Calculated Fe-W phase diagram (Jacob et al. 2015).

To characterize the relationship between the steel chemical composition and the tungsten-steel joint structure, iron and various steels were melted on a tungsten substrate according to the modes from the wetting experiment. The interaction between iron and tungsten represents the simplest case, thus we will begin the discussion with it. Furthermore, the simple Fe-W composition allows for the determination of the phase composition via the binary phase diagram.

Microstructure images of SEM of iron melted on tungsten at 1550 °C are shown in Fig. 5. Due to the high number of microstructure images, only a few of them are showed in this paper. An interlayer with the typical for as-cast metal dendrite structure covers the tungsten surface. Within iron-based matrix IMC form dendrite structure with various shapes and sizes. As the temperature increases, the dendrite structure in matrix and IMC interlayer becomes thicker. Cracks are distinctly visible at the interface between the tungsten and the interlayer, with some cracks propagating from the outer surface to the interlayer.

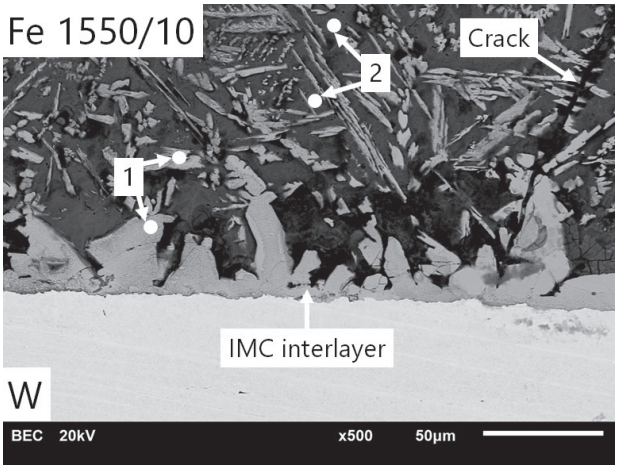

Figure 5. Microstructure of WFe/1550/10.

The chemical composition of the interlayer measured with EDS analysis was studied on the WFe/1550/10 specimen. Point 1 with a composition of 57.3Fe-42.7W at.% is expected to be μ-phase. It should be noted that the μ-phase deviate from stoichiometric composition at the room temperature, which is typical for casted metals The chemical composition of μ-phase corresponds to the equilibrium composition at 800 °C. Point 2 with a composition of 93.9Fe-6.1W at.% corresponds to the iron matrix around μ-phase The chemical compositions of points 1 and 2 are marked on the Fe-W phase diagram in Fig. 4. Light grey phases in the iron matrix have a composition close to the Point 1.

The EDS map of specimens obtained after the long-term exposure at 1600 °C is shown in Fig. 6. It is apparent that Fe does not significantly diffuse into the base W, while tungsten actively dissolves in iron. The high W content at different distances from the joint indicates that diffusion primarily occurs in the liquid state.

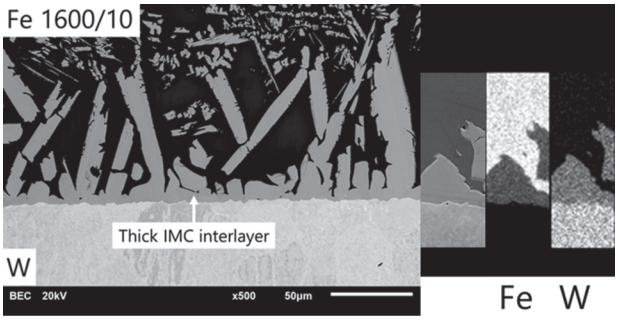

Figure 6. Microstructure and EDS map of WFe/1600/10 specimen.

Due to the extremely low solubility of W in Fe at the room temperature, the equilibrium state consists of α-Fe and the μ-phase. SEM analysis did not reveal the λ phase, which is stable in the temperature range of 150–1100 °C. This phase is expected to form during decomposition of μ and α-Fe due to diffusion in solid state. All phases observed near the joint area exhibit a similar composition close to the μ-phase. The chemical composition of the iron matrix becomes enriched with tungsten content with increasing exposure temperature, indicating that overheated liquid iron actively dissolves tungsten. The matrix of specimens melted at 1550 °C contains 4.3 at.% of W, whereas at 1600 °C it contains 6.3 at.%.

The absence of the Laves λ-phase and the non-equilibrium composition of phases could indicate that cooling suppresses the phase evolution in the steel matrix. When solidification under equilibrium conditions occurs, the matrix should undergo a series of phase transformations: L→α-Fe+μ→α-Fe+λ→α-Fe+μ. At the room temperature, the α-Fe+μ composition is stable.

Interaction between AISI 420, EK-181 and W

The RAFM steel EK-181 does not significantly differ from AISI 420 in chemical composition. The influence of micro-alloying on wetting and interaction is considered negligible. Therefore, main features will be discussed based on the AISI 420 case.

The investigation aims to determine the influence of the steel alloying elements on the structure of the interlayer. AISI 420, characterized by high chromium and carbon content, was melted on a tungsten substrate at 1550 and 1600 °C. The microstructure image of the W420/1600/10 specimen and EDS maps are presented in Fig. 7, revealing a similar dendrite structure. An IMC layer covers the entire surface of tungsten. Notably, no cracks or pores were observed in the W420 joints, in contrast to the WFe case. The modified μ-phase at point 1 with composition of 4Cr-53.3Fe-42.7W at.% contains chromium. Point 2 in the steel matrix with composition of 5.8Cr-89.5Fe-4.7W at.% contains a lower tungsten content than in the case of WFe melted in the same way.

Chromium actively diffuses into the tungsten substrate. Chromium has high solubility in tungsten especially at high temperatures. This is verified by comparing the Cr content in the matrix between melting at 1550 and 1600 °C. Chromium content is 7.8 at.% in the specimens melted at 1550 while melting at 1600 results in the decrease of chromium content down to 5.8 at.%.

The carbon content of 420 steel is the highest among the studied steels. However, detecting carbon with high accuracy is challenging due to its low mass and surface pollution. We assume that carbon affects phase formation primarily due to its high affinity for tungsten. The affinity of W to C is reported to be higher than that of Cr (Jansson and Lewin 2013). While XRD is a common method for determining phase composition, it can be challenging to detect microscopic precipitates using this technique. The peaks observed correspond to α-Fe solid solution, Fe_7W_6, Fe_2W, and Fe oxides detected in the XRD

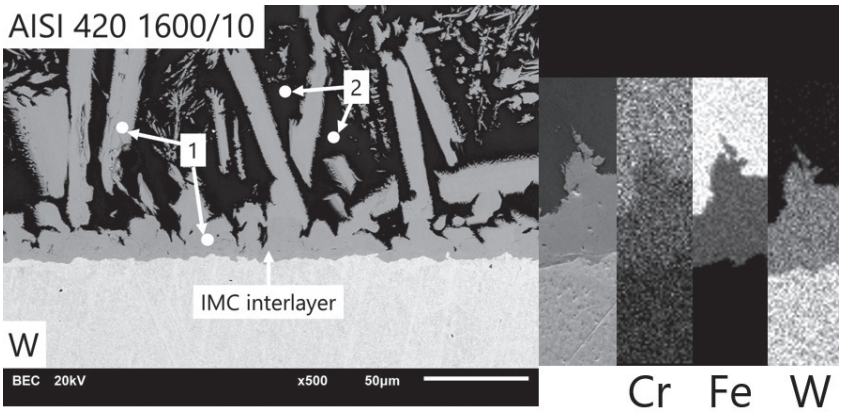

Figure 7. Microstructure of W420/1600/10 specimen.

spectra measured across the entire specimen, including the interlayer and steel matrix zone. Consequently, the phase composition of each individual zone in the joint remains unclear.

To estimate the probable phase composition, thermodynamic calculations were carried out using Thermo-Calc software. Phase composition of tungsten-steel joint zone studied via synchrotron XRD technique. Due to high specimens number only one spectra presented in Fig. 8. The results of phase composition calculation of two points presented in Table 3. Point 1 (Fe-41.5W-5.3Cr-1C at.%) and 2 (Fe-4.5W-7.8C-1C at.%) corresponds to chemical composition of IMC layer and steel matrix respectively. Initial AISI 420 steel contain approximately 1 at.% of carbon. Therefore, all chemical compositions in Thermocalc thermodynamic calculations are alloyed with 1 at.% carbon to evaluate the effect of carbon.

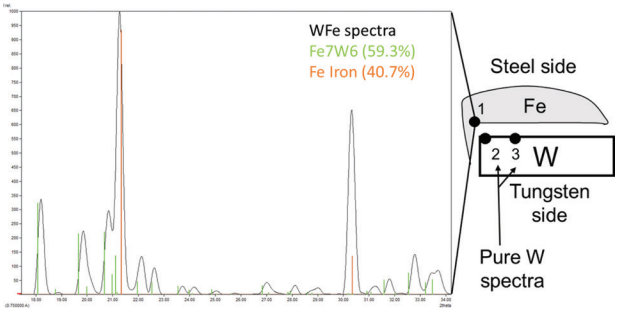

Figure 8. Example of XRD spectra of WFe/1550/10 specimen.

The calculations show that M_6C carbide forms due to the high W-C affinity and remains stable in a broad temperature range. In the high-temperature range, the phase composition primarily consists of the μ-phase. Within the matrix composition, carbon form M_6C and $M_{23}C_6$ type carbide phases. The primary component of the matrix is the α-Fe solid solution. Tungsten and chromium are both strong carbide formers, the absence of Cr and W carbides in the structure indicates that the dissolved carbon or carbides in the matrix are too small to detect. Calculated compositions suggest that the Laves λ-phase is thermodynamically stable at lower temperatures.

Table 3. Phase composition modeling of W420 joint alloyed with carbon

Phase name	Chemical composition, at.%	Equilibrium composition	Experimental data from XRD
IMC layer	Fe-41.5W-5.3Cr-1C	μ-phase, λ-phase, M_6C	α-Fe, μ-phase, λ-phase (traces)
Steel matrix	Fe-4.5W-7.8C-1C	α-Fe, λ-phase, $M_{23}C_6$	

Comparison of the XRD results and calculations leads to the conclusion that the W420 joint consists of μ-phase, α-Fe matrix, and Laves λ-phase. The absence of carbides in the XRD analysis is attributed to their small size and technical constraints. Traces of the Laves phase indicate that its content and size are insufficient for reliable analysis. In comparison with data obtained by casting steel at 1550 °C in (Kumar 2013) we can conclude that Laves λ-phase does not play significant role in intermetallic layer structure. Due to lower W content in λ-phase they most likely to form in steel matrix away from W wire.

Interaction between W and AISI 316L

The second steel type contains Ni and Cr, while the carbon content is low. Steel 316L also has a low melting point, allowing us to utilize an additional mode without exposure at 1500 °C (immediate cooling after rapid heating). However, no difference in microstructure was observed between specimens with and without 1-minute exposure. The microstructure of steel 316L melted on tungsten at 1500 and 1600 °C for 0 and 10 minutes, respectively, is shown in Fig. 9.

High-temperature exposure with overheating by 150 °C (W316/1550 specimen) above the melting point results in significant erosion of tungsten grains by the liquid metal. A W cluster exceeding 50 μm in size was detected in the steel matrix. Further away from the joint zone, a fine grid structure was observed. Conversely, overheating by approximately 100 °C above the melting temperatures only leads to the growth of the dendritic structure.

The thickness of the intermediate joint layer at 1500 °C is about 5 μm. Point 1 (marked in Fig. 9a) has composition of 12.3Cr-45.3Fe-3.9Ni-38.5W at.%, which is presumed to be a modified μ-phase. Nickel was not detected deep

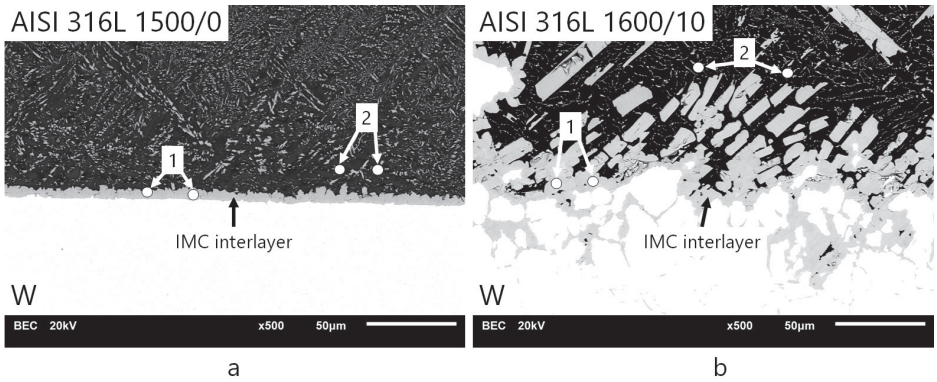

Figure 9. Microstructure of W316/1500/0 and W316/1600/1 specimens.

in the bulk tungsten, while chromium actively diffuses at all studied temperatures. Point 2 corresponds to a steel matrix with composition of 16.3Cr-68.2Fe-11.2Ni-4.3W at.%. Matrix has a high tungsten content; the content of other elements remains at the same level.

The maps of chemical elements distribution shown in Fig. 10 illustrate the erosion process in the case of the W316/1600/10 sample, where liquid steel actively dissolves the tungsten grain boundaries. Point 1 in Fig. 9b has a composition of 3.5Cr-48.9Fe-5.1Ni-42.5W at.%. It is evident that the Cr content is significantly lower in the μ-phase, while Ni content has increased compared to the W316/1500/0. The steel matrix at point 2 has a low Cr content of about 4.5 at.%. A fine grid of Cr-based phases is observed in both the EDS maps and the SEM image.

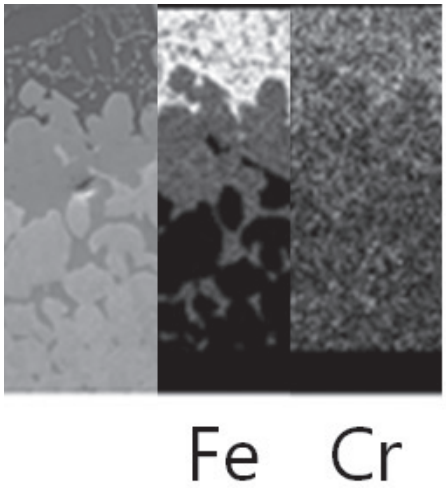

Figure 10. EDS map of W316/1600/10 specimen.

The phase composition of W316 specimens studied in the same way as W420. For thermodynamic calculations two compositions were used: Fe-41W-7Cr-4Ni at.% (IMC layer) and Fe-5W-9Cr-13Ni at.% (steel matrix). Calculations presented in Table 4 show that the equilibrium composition for steel matrix is a mixture of γ-Fe and α-Fe solid solutions with λ-phase, while IMC layer has composition of μ-phase, λ-phase with some γ-Fe additions. The XRD results shows clear peaks of γ-Fe and μ-phase, while α-Fe and λ-phase remain undetected.

Table 4. Phase composition modeling of W316 joint alloyed with carbon

Phase name	Chemical composition, at.%	Equilibrium composition	Experimental data from XRD
IMC layer	Fe-41W-7Cr-4Ni	μ-phase, λ-phase, γ-Fe	γ-Fe, μ-phase
Steel matrix	Fe-5W-9Cr-13Ni	α-Fe, γ-Fe, λ-phase	

Phase evolution

The microstructure evolution stages are presented in a schematic representation in Fig. 11. Two types of interaction with the melt have been established: diffusion and erosion. Both steels AISI 420, EK-181 and iron exhibit similar behaviors when interacting with tungsten, resulting in the formation of a dendritic structure with varying thickness in the interaction zone. A layer of μ-phase IMC composed of Fe, W, and Cr covers the surface of tungsten.

IMC layer is formed during interaction of the melt with solid tungsten due to relatively slow diffusion process on the solid/liquid boundary The liquid near the boundary becomes enriched with W, which raises the melting point, leading to nucleation of a μ-phase on the surface of tungsten. The W-Fe diagram shown in Fig. 12 can be used to define the composition of liquid and solid structure. In this stage liquid near W form diffusion layer with composition close to C_L point in Fig. 12. When W content increase due to diffusion, the solid μ-phase nucleate. IMC start to grow in form of dendrites forming solidification front. The chemical composition of μ-phase corresponds to C_s point in diagram. Diffusion layer quickly propagates due to high diffusion rate in liquid state. Described process undergo until cooling starts.

Cooling cause fast temperature drop. Thus, C_L point shifts to C'_s which means that liquid crystallize in form of α-Fe enriched with W. After that follows decomposition with μ-phase grow in α-Fe. The composition of α-Fe change according solvus from point C'_s to C''_s. The EDS data evidence that ~5 at.% of W remains in steel, which means that diffusion after 1100 °C is weak. The composition of μ-phase remains close to C_s due to the fact that it is stable composition for wide range of temperatures.

When overheating exceeds 150 degrees (W316 specimens melted at 1500 and 1600 °C) selective dissolution of

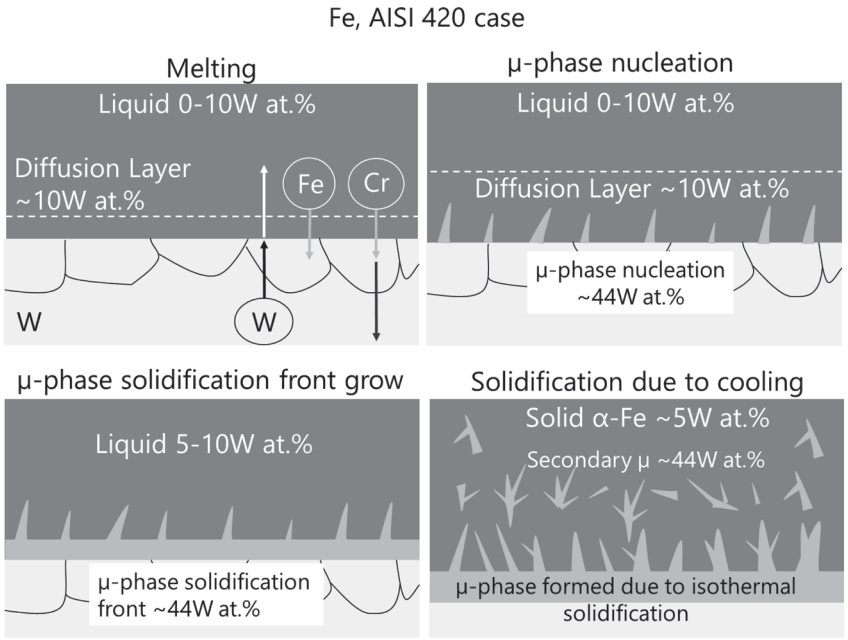

Figure 11. Schematic illustration of liquid melt interaction with W.

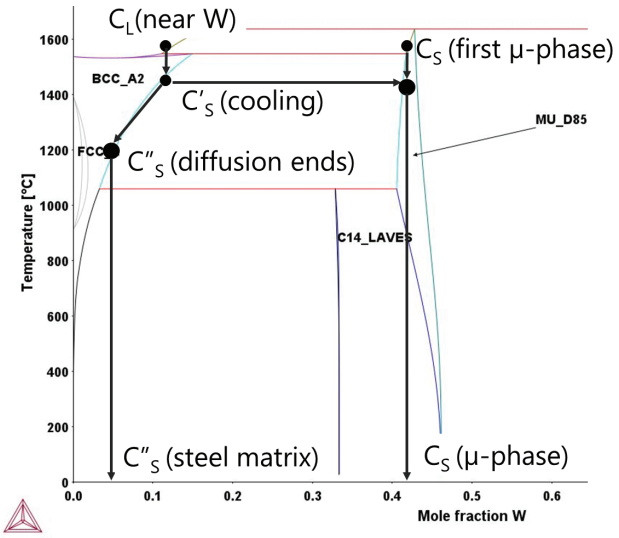

Figure 12. Fe corner of W-Fe diagram.

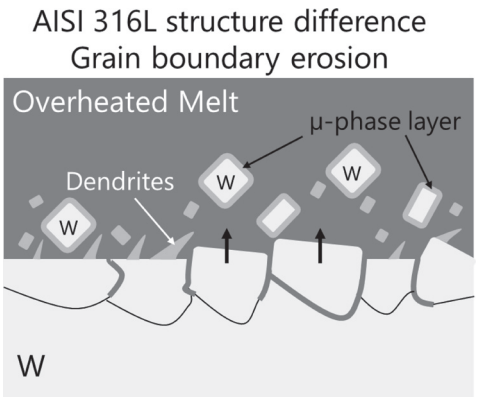

Figure 13. Tungsten grain boundary erosion by liquid AISI 316L melt.

grain boundaries occur. This feature illustrated in Fig. 13. The liquid melt separates single grain, absorbs it and dissolves it. This process, previously observed in studies of corrosion of refractory alloys (Lyutyi et al. 1991), is associated with the grain boundaries energy and impurities in them.

Cooling down at a relatively high rate follows the exposure. When cooling under furnace conditions, the temperature drops from 1550–1600 to 1300 °C at an approximate rate of 100 °C/min. As a result, solidification occurs immediately after the exposure ends. The liquid steel, enriched with tungsten, solidifies as an α-Fe solid solution of non-equilibrium composition.

After solidification, diffusion rate significantly drops, resulting in minimal changes in the distribution of chemical elements. The stage of solid phase decomposition is characterized by a low cooling rate, which decreases exponentially over time. Consequently, phase decomposition occurs partially. During decomposition, a secondary μ-phase nucleates in the steel matrix. According to XRD λ-phase precipitates only in the W420 joint.

Results application and future work

The results obtained demonstrate that iron and steel perfectly wet the tungsten surface. The capillary forces are strong enough to wet not only the polished face but also the back side of the tungsten plate. In this experiment, tungsten and steel were heated to the same temperature. Under these isothermal conditions, wetting occurs simultaneously. However, in real liquid metal injection technology, the tungsten mesh might have a lower temperature than the liquid steel, which would prevent undesirable interaction and lead to obtaining an optimal structure.

To achieve this, several issues need to be considered. The first is the interaction of melted steel with tungsten at a lower temperature. This can be addressed by injecting melted steel onto a tungsten substrate, heated separately to a different temperature. Sessile drop method allow to measure wetting angle of steel melt at various substrates heated to lower temperature (Long et al. 2024).

The second issue to consider is the use of barrier layers, which might completely prevent the interaction. A layer such as tungsten carbide (WC, W_2C, α-WC_{1-x}) appears to meet wetting, CTE and thermal conductivity requirements (Reeber and Wang 1999; Zhou et al. 2003; Tripathy et al. 2022). Thermodynamic calculations show that M_6C carbide is formed at high carbon content and is thermodynamically stable until the steel is melted. If the carbide layer is thin enough, the effect on thermal conductivity is negligible. Oxide and nitride ceramics are strictly prohibited due to their interaction with Li under tokamak conditions. Corrosion resistance in liquid metal environment comes from the expected conditions of tokamak with reactor technologies (Mazul et al. 2021).

The actual structure of tungsten mesh infiltrated with steel melt depend on the mesh size, thickness and temperature of W wire, temperature of steel melt. During infiltration the steel melt temperature will inevitably decrease to solidus. Intermetallic layer on W wire could block capillaries between wires if the rate of IMC grow is higher than the rate of colling.

Conclusion

The investigation focuses on the wetting characteristics and joint structure of tungsten with iron, EK-181, AISI 420, and 316L steels under isothermal conditions. High-temperature wetting at 1500–1600 °C reveals that all the studied materials perfectly wet the W substrate. The interaction between the melt and solid tungsten leads to the formation of a dendritic structure with a μ-phase at the solid/liquid boundary. The melt solidifies in the form of a solid solution enriched with tungsten, resulting in decomposition with the nucleation of μ and λ-phases in the iron and AISI 420 steel matrices. For the 316L steel, γ-Fe, μ-phase and α-Fe are formed.

The interaction rate primarily depends on overheating of melt. The 150 °C of overheating appears to be critical point, when erosion type of interaction overcomes the diffusion type. The results show that undesired interaction might be completely suppressed by diffusion barrier layers.

Funding

This work has been supported by the grants the Russian Science Foundation, RSF 24-2300111

Sample characterization using the Synchrotron was done with the support of the Ministry of Science and Higher Education of the Russian Federation (Agreement No. 075-15-2021-1352).

References

- Andruczyk D, Maingi R, Hu JS, Zuo GZ, Rizkallah R, Parsons M, Shone A, O'Dea D, Kapat A, Szott M, Stemmley S, Sun Z, Xu W, Meng XC, Lunsford R, Gilson EP, Diallo A, Tritz K, The EAST team (2020) Overview of lithium injection and flowing liquid lithium results from the US–China collaboration on EAST. Physica Scripta T171: 014067. https://doi.org/10.1088/1402-4896/ab6ce1
- Bachurina D, Suchkov A, Gurova J, Kliucharev V, Vorkel V, Savelyev M, Somov P, Sevryukov O (2021a) Brazing Tungsten/Tantalum/RAFM Steel Joint for DEMO by Fully Reduced Activation Brazing Alloy 48Ti-48Zr-4Be. Metals 11: 1417. https://doi.org/10.3390/met11091417
- Bachurina D, Suchkov A, Gurova J, Savelyev M, Dzhumaev P, Kozlov I, Svetogorov R, Leont'eva-Smirnova M, Sevryukov O (2021b) Joining tungsten with steel for DEMO: Simultaneous brazing by Cu-Ti amorphous foils and heat treatment. Fusion Engineering and Design 162: 112099. https://doi.org/10.1016/j.fusengdes.2020.112099
- Chen H, Ye L, Han Y, Chen C, Fan J (2021) Additive manufacturing of W–Fe composites using laser metal deposition: Microstructure, phase transformation, and mechanical properties. Materials Science and Engineering: A 811: 141036. https://doi.org/10.1016/j.msea.2021.141036
- Chen Z, Sawa Y, Hashimoto N (2018) Development of F82H composite materials with a high thermal conductivity. Nuclear Materials and Energy 16: 133–136. https://doi.org/10.1016/j.nme.2018.06.017
- Dandliker RB, Conner RD, Johnson WL (1998) Melt infiltration casting of bulk metallic-glass matrix composites. Journal of Materials Research 13: 2896–2901. https://doi.org/10.1557/JMR.1998.0396
- De Jongh PE, Eggenhuisen TM (2013) Melt Infiltration: an Emerging Technique for the Preparation of Novel Functional Nanostructured Materials. Advanced Materials 25: 6672–6690. https://doi.org/10.1002/adma.201301912
- De Luca R, Fanelli P, Paoletti D, Stefanini C, Von Müller A, Feichtmayer A, Vivio F, Belardi V, Dose G, De Sano G, Roccella S, Calabro G, You J-H, Neu R (2023) Pre-conceptual design of a PFC equipped with a W lattice armour for first wall limiters in the EU-DEMO fusion reactor. Fusion Engineering and Design 191: 113742. https://doi.org/10.1016/j.fusengdes.2023.113742
- Fabritsiev SA, Zinkle SJ, Singh BN (1996) Evaluation of copper alloys for fusion reactor divertor and first wall components. Journal of Nuclear Materials 233–237: 127–137. https://doi.org/10.1016/S0022-3115(96)00091-8
- Gago M, Kreter A, Unterberg B, Wirtz M (2020) Synergistic effects of particle and transient heat loads on ITER-grade tungsten. Physica Scripta 2020: 014007. https://doi.org/10.1088/1402-4896/ab3bd9
- Ganesh V, Dorow-Gerspach D, Bram M, Coenen JW, Wirtz M, Pintsuk G, Theisen W, Linsmeier C (2023) Processing and Properties of Sintered W/Steel Composites for the First Wall of Future Fusion Reactor. Journal of Nuclear Engineering 4: 177–192. https://doi.org/10.3390/jne4010014
- Gao WJ, Zhang WW, Zhang T, Yang C, Huang XS, Liu ZY, Wang Z, Li WH, Li WR, Li L, Liu LH (2021) Large tensile plasticity in Zr-based metallic glass/stainless steel interpenetrating-phase composites prepared by high pressure die casting. Composites Part B: Engineering 224: 109226. https://doi.org/10.1016/j.compositesb.2021.109226

- Guseva MI, Suvorov AL, Korshunov SN, Lazarev NE (1999) Sputtering of beryllium, tungsten, tungsten oxide and mixed W–C layers by deuterium ions in the near-threshold energy range. Journal of Nuclear Materials 266–269: 222–227. https://doi.org/10.1016/S0022-3115(98)00819-8
- Heuer S, Li B-S, Armstrong DEJ, Zayachuk Y, Linsmeier Ch (2020) Microstructural and micromechanical assessment of aged ultra-fast sintered functionally graded iron/tungsten composites. Materials & Design 191: 108652. https://doi.org/10.1016/j.matdes.2020.108652
- Hirai T, Ezato K, Majerus P (2005) ITER Relevant High Heat Flux Testing on Plasma Facing Surfaces. MATERIALS TRANSACTIONS 46: 412–424. https://doi.org/10.2320/matertrans.46.412
- Jacob A, Schmetterer C, Singheiser L, Gray-Weale A, Hallstedt B, Watson A (2015) Modeling of Fe–W phase diagram using first principles and phonons calculations. Calphad 50: 92–104. https://doi.org/10.1016/j.calphad.2015.04.010
- Jansson U, Lewin E (2013) Sputter deposition of transition-metal carbide films — A critical review from a chemical perspective. Thin Solid Films 536: 1–24. https://doi.org/10.1016/j.tsf.2013.02.019
- Koller M, Kruisová A, Mušálek R, Matějíček J, Seiner H, Landa M (2018) On the relation between microstructure and elastic constants of tungsten/steel composites fabricated by spark plasma sintering. Fusion Engineering and Design 133: 51–58. https://doi.org/10.1016/j.fusengdes.2018.05.056
- Kumar P (2013) Studies Of Wire-Matrix Interaction In Some Tungsten Wire Reinforced Stainless Steels. University of Canterbury
- Lazurenko DV, Ivannikov AA, Anisimov AG, Popov NS, Emurlaev KI, Dovzhenko GD, Bataev IA, Kuzmin RI, Kuper KE (2024) Structure and mechanical properties of three-layer composites obtained by magnetic pulse welding of titanium and Zr-based metallic glass. The International Journal of Advanced Manufacturing Technology. https://doi.org/10.1007/s00170-024-13484-0
- Long Q, Wang W, Gao X (2024) Measuring Dynamic Nonreactive Wetting Behavior Between Interstitial-Free Molten Steel and Alumina. Metallurgical and Materials Transactions B. https://doi.org/10.1007/s11663-024-03065-7
- Lyublinski IE, Vertkov AV, Zharkov MY, Sevryukov ON, Dzhumaev PS, Shumskiy VA, Ivannikov AA (2016) Selection of materials for tokamak plasma facing elements based on a liquid tin capillary pore system. Journal of Physics: Conference Series 748: 012014. https://doi.org/10.1088/1742-6596/748/1/012014
- Lyutyi EM, Eliseeva OI, Bobyk RI (1991) Corrosion of refractory metals and alloys in liquid lithium (a review). Soviet Materials Science 26: 611–621. https://doi.org/10.1007/BF00723645
- Mazul IV, Giniyatulin RN, Kavin AA, Litunovskii NV, Makhankov AN, Piskarev PYu, Tanchuk VN (2021) Plasma-Facing Components of the TRT Tokamak. Plasma Physics Reports 47: 1220–1237. https://doi.org/10.1134/S1063780X21110210
- Meng X, Zuo G, Sun Z, Xu W, Huang M, Xu C, Qian Y, Hu W, Hu J, Deng H (2018) Compatibility of Molybdenum, Tungsten, and 304 Stainless Steel in Static Liquid Lithium Under High Vacuum. Plasma Physics Reports 44: 671–677. https://doi.org/10.1134/S1063780X18070036
- Paúl A, Beirante A, Franco N, Alves E, Odriozola JA (2006) Phase Transformation and Structural Studies of EUROFER RAFM Alloy. Materials Science Forum 514–516: 500–504. https://doi.org/10.4028/www.scientific.net/MSF.514-516.500
- Penyaz MA, Ivannikov AA, Sevryukov ON, Kalin BA (2021) Overview of nickel-based filler metals for brazing of austenitic stainless steels. Non-ferrous Metals: 41–56. https://doi.org/10.17580/nfm.2021.01.06
- Qu DD, Wirtz M, Linke J, Vaßen R, Aktaa J (2019) Thermo-mechanical response of FG tungsten/EUROFER multilayer under high thermal loads. Journal of Nuclear Materials 519: 137–144. https://doi.org/10.1016/j.jnucmat.2019.03.019
- Reeber RR, Wang K (1999) Thermophysical Properties of α-Tungsten Carbide. Journal of the American Ceramic Society 82: 129–135. https://doi.org/10.1111/j.1151-2916.1999.tb01732.x
- Saito S, Fukaya K, Ishiyama S, Sato K (2002) Mechanical properties of HIP bonded W and Cu-alloys joint for plasma facing components. Journal of Nuclear Materials 307–311: 1542–1546. https://doi.org/10.1016/S0022-3115(02)01169-8
- Schoofs F, Gorley M (2019) A route to standardised high heat flux testing: An example for tungsten. Fusion Engineering and Design 139: 132–136. https://doi.org/10.1016/j.fusengdes.2018.12.060
- Tan C, Zhou K, Kuang T (2019) Selective laser melting of tungsten-copper functionally graded material. Materials Letters 237: 328–331. https://doi.org/10.1016/j.matlet.2018.11.127
- Tolias P (2017) Analytical expressions for thermophysical properties of solid and liquid tungsten relevant for fusion applications. Nuclear Materials and Energy 13: 42–57. https://doi.org/10.1016/j.nme.2017.08.002
- Toy C, Scott WD (1990) Ceramic-Metal Composite Produced by Melt Infiltration. Journal of the American Ceramic Society 73: 97–101. https://doi.org/10.1111/j.1151-2916.1990.tb05097.x
- Tripathy H, Sudha C, Paul VT, Thirumurugesan R, Prasanthi TN, Sundar R, Vijayashanthi N, Parameswaran P, Raju S (2022) High temperature thermophysical properties of spark plasma sintered tungsten carbide. International Journal of Refractory Metals and Hard Materials 104: 105804. https://doi.org/10.1016/j.ijrmhm.2022.105804
- Weber T, Stüber M, Ulrich S, Vaßen R, Basuki WW, Lohmiller J, Sittel W, Aktaa J (2013) Functionally graded vacuum plasma sprayed and magnetron sputtered tungsten/EUROFER97 interlayers for joints in helium-cooled divertor components. Journal of Nuclear Materials 436: 29–39. https://doi.org/10.1016/j.jnucmat.2013.01.286
- Xuan C, Shibata H, Zhao Z, Jönsson PG, Nakajima K (2015) Wettability of TiN by Liquid Iron and Steel. ISIJ International 55: 1642–1651. https://doi.org/10.2355/isijinternational.ISIJINT-2014-819
- Yan W, Schmidt A, Dudczig S, Wetzig T, Wei Y, Li Y, Schafföner S, Aneziris CG (2018) Wettability phenomena of molten steel in contact with alumina substrates with alumina and alumina-carbon coatings. Journal of the European Ceramic Society 38: 2164–2178. https://doi.org/10.1016/j.jeurceramsoc.2017.12.001
- Yang Q, Chen Z, Du Q, Xu H, Zuo G, Ren J, Hu J, Song Y, Li J, Ding F, Zakharov L (2017) Development of the flowing liquid lithium limiter for EAST tokamak. Fusion Engineering and Design 124: 179–182. https://doi.org/10.1016/j.fusengdes.2017.04.063
- Zhou R, Jiang Y, Lu D (2003) The effect of volume fraction of WC particles on erosion resistance of WC reinforced iron matrix surface composites. Wear 255: 134–138. https://doi.org/10.1016/S0043-1648(03)00290-4
- Zuo GZ, Hu JS, Li JG, Luo NC, Zakharov LE, Zhang L, Ti A (2011) First results of lithium experiments on EAST and HT-7. Journal of Nuclear Materials 415: S1062–S1066. https://doi.org/10.1016/j.jnucmat.2010.08.052